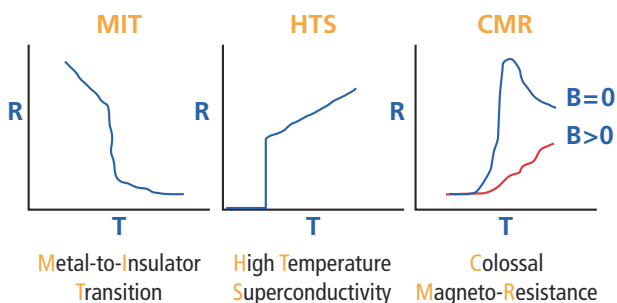# V. Time-Resolved Spectroscopy of Correlated Electron Materials

Mapping the flow of energy among strongly-coupled degrees of freedom

- Correlated electron phases

- X-ray methods in correlated electron science

- The origin of the metal-insulator transition in TaS_2

- Ultrafast investigations of the electron-phonon interaction

- Complexity in correlated electron materials

"Electron correlation" is a dominant theme in condensed matter science, manifesting itself in, e.g., "metal-insulator transitions" (MIT), "high-temperature superconductivity" (HTS) and "colossal magneto-resistance" (CMR). On the microscopic scale, one speaks of the charge (C), spin (S) and orbital (O) degrees of freedom, each of which may show short- or long-range order, and each of which may exchange energy with the others and with the crystal lattice (L) (see Fig. V.1). Important correlation effects can occur in systems with partially-filled electron shells, such as those of 3d-transition metal ions, with anisotropic, quasi-localized character. Vast amounts of experimental and theoretical work have been published on electron correlation, triggered largely by the discovery of HTS in 1986 [2]. Phase diagrams of many interesting materials have been investigated in detail, and numerous theories of the microscopic charge-spin-orbital-lattice interactions have been proposed. Much has been achieved, but much is still unclear. There is increasing evidence of the importance of nanoscale inhomogeneities and fast fluctuations in correlated electron materials – indicating the important role that the SwissFEL will play. Furthermore, it has been suggested that the chicken-or-egg problem, of determining the cause and effect relationships among the C, S, O and L subsystems, may best be approached with pump-probe time-resolved spectroscopy: one pumps energy into a particular degree of freedom and measures the time required for a response to appear in the others.

a)

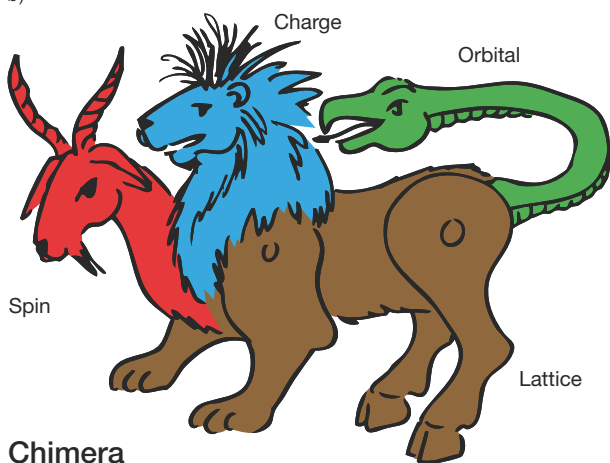| MIT	HTS	CMR
Metal-to-Insulator Transition	High Temperature Superconductivity	Colossal Magneto-Resistance

b)

Charge

Orbital

Spin

Lattice

Chimera

Fig. V.1. a) Three macroscopic manifestations of correlated electrons, with strong potential for important applications. b) The Charge-Spin-Orbital-Lattice "Chimera" of correlated electron science [1], which emphasizers the interrelated degrees of freedom. The Chimera is a beast from Greek mythology.
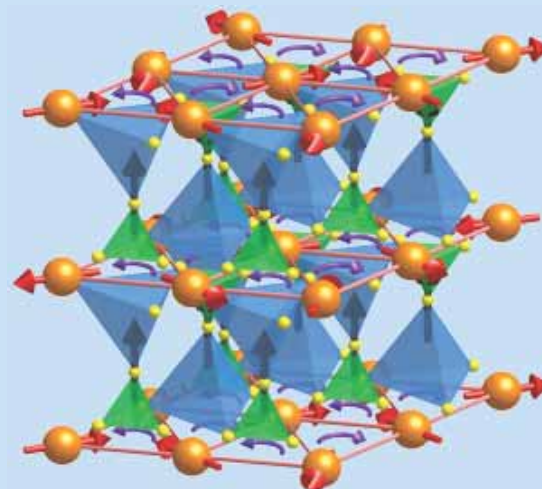
Multiferroic materials

Fig. V.i1. The multiferroic material RbFe(MoO$_4$)$_2$.

Order parameters that can be switched between and "up" and "down" states are called ferroic. If a material has simultaneously two ferroic order paramaters, then it is called multiferroic. This definition has been somewhat relaxed in the past few years, and it has now customary to call any material multiferroic that shows spontaneous magnetic order and ferroelectricity [24]. An example is when a material has a spontaneous dipole moment and antiferromagnetic order. Because multiple order parameters are almost always coupled, multiferroic materials hold the promise that the electric dipole moment can be manipulated magnetically, or that ferromagnetic magnetization can be manipulated electrically, with exciting possibilities for novel device applications involving ultrafast switching.

There are different mechanisms that can lead to the simultaneous presence of ferroelectricy and magnetic order. One of the simplest is when ferroelectricity emerges directly from magnetic order. This can happen when magnetic order breaks the symmetry in such a way that a switchable electric polarization occurs. There are other mechanisms, such as geometric ferroelectrics and lone-pair ferroelectrics, which are as yet not fully understood. The most interesting and promising cases are materials in which ferroelectricity arises from charge frustration which is coupled with magnetism (see Fig. V.i1). This can lead to a large electric polarization and strong coupling effects at high temperature. There are only few such electronic ferroelectrics known to date, and their physics is presently under intense investigation.

Correlated electron phases

A prominent class of correlated electron materials are transition-metal oxides (TMO), based on the perovskite crystal structure, with transition-metal ions in octahedral environments. Figure V.2 indicates, using the example of Mn^{3+} and Mn^{4+}, the splitting of the 3d-electron energy levels caused by the octahedral crystal-field and the Jahn-Teller distortion (see also Chapters I and II). Note that a large correlation energy causes both ions to be in the Hund's rule "high-spin" state.
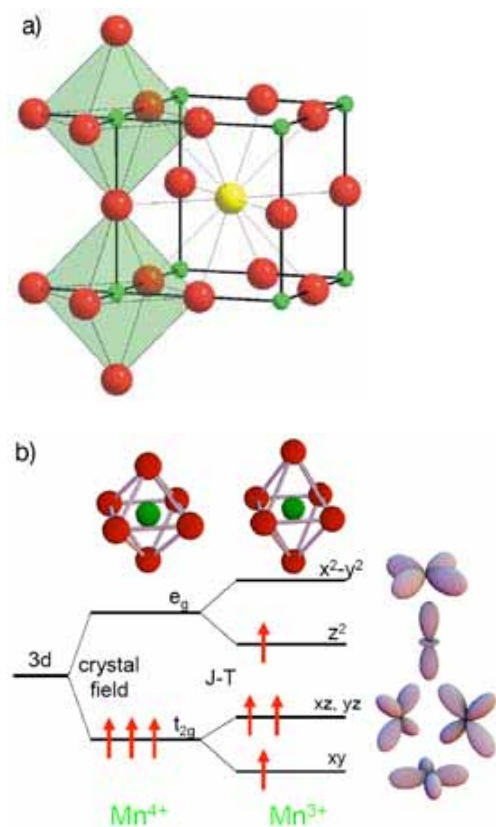

Fig. V.2. a) The undistorted ABO_3 perovskite structure, showing the green transition-metal ions (B) at the center of O^{2-} octahedra. b) Energy splitting of the 3d-electron states in an octahedral crystal field (Mn^{4+}) and due to the Jahn-Teller effect (Mn^{3+}).

TMO materials show ordered phases of the charge, spin and orbital degrees of freedom; Figure V.3 indicates the different unit cells which occur in the MnO_2 planes of the manganite $La_{0.5}Sr_{1.5}MnO_4$ [3].

An example of the variety of phases which arise in TMOs is that of the manganite $La_{1-x}Ca_xMnO_3$ (LCMO) (see Fig. V.4 a) [4]. As the electron concentration is increased by Ca doping, the stable low-temperature phase changes from antiferromagnetic insulator (AFI), to ferromagnetic insulator (FMI), to ferromagnetic metal (FMM) and finally

to a charge-orbitally ordered state (CE). In the FMM phase of LCMO, colossal magnetoresistivity is associated with the formation of nanoscale polarons that develop at elevated temperature, which, around $x \approx 0.3$, show correlations with a wave-vector $\approx$ (¼, ¼, 0) [3]. These correlations develop into long-range order at $x \approx 0.5$, where equal numbers of Mn^{3+} and Mn^{4+} form a charge- and orbitally-ordered structure known as "CE". Above the magnetic ordering temperature, a correlated polaron glass phase is formed, with a weakly temperature-dependent correlation length in the nanometer range. At still higher temperature, these static polarons become purely dynamic in character, as evidenced by inelastic neutron scattering (see Fig. V.4 b).
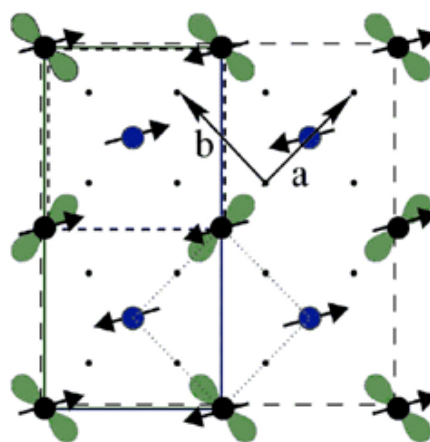

Fig. V.3. The unit cells in the MnO_2 planes of the layered material $La_{0.5}Sr_{1.5}MnO_4$ [3]. The small dots are O^{2-}, and the large black and blue dots represent Mn^{3+} and Mn^{4+} ions, respectively. One distinguishes the $I4/mmm$ crystallographic (dots), the charge (small dashes), the orbital (solid) and the magnetic (large dashes) unit cells.

Another famous example of correlated-electron TMOs are the cuprates showing high-temperature superconductivity. The crystal structure and (schematic) phase diagram for $YBa_2Cu_3O_{7-x}$, a hole-doped superconductor, are shown in Figure V.5. CuO_2 planes in the layered, oxygen-deficient perovskite structure are responsible for superconductivity. Besides the superconducting phase (SC), of particular interest in the "underdoped" regime, are the spin-glass (SG) and pseudo-gap regions. Here there is evidence that static and dynamic "stripes" occur, with characteristic arrangements of Cu-ion charge and spin on the nanometer scale [5].
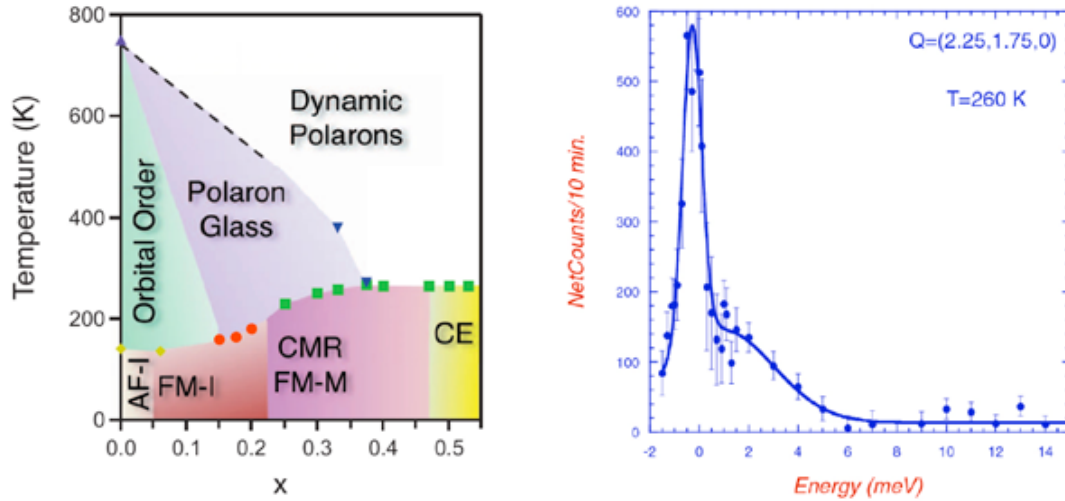
Fig. V.4. a) The phase diagram of $La_{1-x}Ca_xMnO_3$, as a function of the electron doping x [4]. The antiferromagnetic insulator (AFI) and the ferromagnetic insulator (FMI) and metal (FMM) phases show magnetic order. Charge and orbital order occur in the FMM and CE phases, while orbital order is also found near $x = 0$ above 140 K. Disordered polarons of the CE-type occur above the magnetic ordering temperatures, with spatial correlations on the nanometer scale. b) In the "dynamic" region, inelastic neutron scattering shows the polarons to be fluctuating on the ps time-scale, as evidenced by the inelastic shoulder at the right of the $E = 0$ elastic scattering peak.
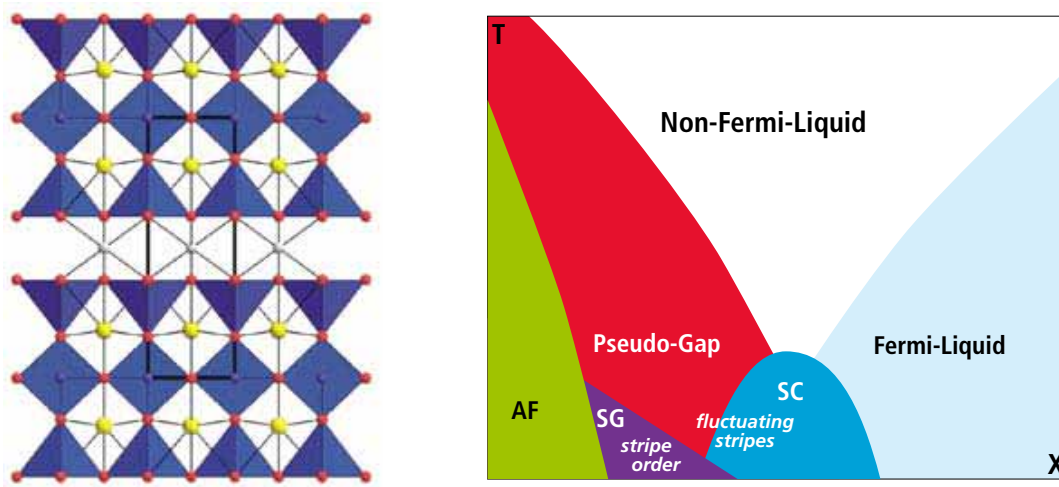

Fig. V.5. a) The layered perovskite structure of $YBa_2Cu_3O_{7-x}$, with the superconducting CuO_2 planes perpendicular to the plane of the figure. b) The schematic phase diagram of hole-doped high-temperature superconductors with, among others, the antiferromagnetic (AF), spin-glass (SG) and superconducting (SC) phases.

X-ray methods in correlated electron science

The relevance for correlated-electron materials of ps dynamics at the nanoscale, together with strong interaction of X-ray photons with all four of the C-S-O-L degrees of freedom, promises important applications of the SwissFEL. To begin the discussion of relevant X-ray techniques, we consider the Hamiltonian describing an X-ray photon field interacting with the electrons in the sample [6, 7]. For the moment, we treat a single free electron, without spin:

$$H = \frac{\left(\vec{p} - e\vec{A}\right)^2}{2m} + H_{\text{radiation}},$$

where $H_{\text{radiation}} = \sum_{\epsilon,\vec{k}} \hbar\omega_k \left(a_{\epsilon\vec{k}}^\dagger a_{\epsilon\vec{k}} + \frac{1}{2}\right)$ describes photons in the radiation field, with wavevector $\vec{k}$ and polarization ϵ. Expanding the expression for H, we obtain:

$$H = H_{\text{electron}} + H_{\text{interaction}} + H_{\text{radiation}}$$

$$H_{\text{electron}} = \frac{p^2}{2m}$$

$$H_{\text{interaction}} = \frac{e^2 A^2}{2m} - \frac{e\vec{A} \bullet \vec{p}}{m} \equiv H_1 + H_2$$

The interaction Hamiltonian, $H_{\text{interaction}}$, is responsible for producing transitions from an initial state $|i\rangle$ to a final state $|f\rangle$ of the combined system of X-rays and sample. According to Fermi's Golden Rule, the transition rate is given by:

$$w = \frac{2\pi}{\hbar} \left| \langle f|H_1|i\rangle + \sum_n \frac{\langle f|H_2|n\rangle\langle n|H_2|i\rangle}{E_0 - E_n + \hbar\omega_k} \right|^2 \delta\left(\left(\hbar\omega_k - \hbar\omega_{k'}\right) - \left(E_f - E_0\right)\right)$$

Here we are interested in "photon-in" (k) to "photon-out" (k') transitions – thus we include only those terms which are quadratic in the vector potential A. We disregard the linear terms, which are responsible for photoemission. The transition rate is proportional to the square of the "scattering factor", $w \propto \left|S\left(\vec{Q},\omega\right)\right|^2$, which, in turn, is a function of the momentum and energy transfers $\vec{Q} = \vec{k}' - \vec{k}$ and $\omega = \omega_{k'} - \omega_k$.

Consider now the following cases:

Hard X-ray diffraction

If the photon energy $\hbar\omega_k$ is much larger than the excitation energies E_n-E_0 of the system, we need only consider the first matrix element in the expression for w:

$$\langle f|H_1|i\rangle \propto \sum_j \langle 0|e^{i\vec{Q}\bullet\vec{r}_j}|0\rangle = S\left(\vec{Q},0\right) = F\left(\vec{Q}\right)$$

where $|0\rangle$ is the ground-state of the system, and where we now sum over *all* the electrons, with coordinates $\vec{r}_j$. For a crystalline sample, the scattering factor $F\left(\vec{Q}\right)$, is written

$$F\left(\vec{Q}\right) = \sum_{l,m,n} e^{i\vec{Q}\bullet\vec{R}_{lmn}} \sum_{i=1}^{I} e^{i\vec{Q}\bullet\vec{r}_i} f_i\left(\vec{Q}\right),$$

i.e., as a lattice sum over the unit cells and a "structure-factor" sum over the I atoms per unit cell. The quantity $f_i\left(\vec{Q}\right)$ is known as the atomic scattering factor. For a perfect crystal, the lattice sum dictates that F is non-zero only if $\vec{Q} = \vec{G}_{hkl}$, a reciprocal lattice vector. This is the condition for Bragg scattering, which, using the relations $Q = \frac{4\pi\sin\theta}{\lambda}$ and $G = \frac{2\pi}{d}$, can be expressed as Bragg's law: $\lambda = 2d\sin\theta$. We thus see that diffraction at the Bragg angle θ is possible when the X-ray wavelength λ is shorter than twice the lattice-plane spacing (2d). The scattered intensity at the Bragg condition is proportional to $\left|F\left(\vec{Q}\right)\right|^2$. The sensitivity of the Bragg condition to the lattice parameters implies that the diffraction of short X-ray pulses can be used to directly observe lattice phonons.

Soft X-ray resonant diffraction

If the incoming photon energy lies close to an atomic absorption edge, it is the second-order contribution from H_2 which dominates the scattering rate. The case of elastic scattering, $\omega_{k'} - \omega_k = 0$, is treated via an energy-dependent correction to the atomic scattering factor:

$$f_i\left(\vec{Q}\right) \Rightarrow f_i\left(\vec{Q},\omega\right) = f_i\left(\vec{Q}\right) + \Delta f_i\left(\vec{Q},\omega\right),$$

where the correction term obeys:

$$\Delta f_i \propto \sum_n \frac{\left\langle 0 \left| \vec{\epsilon} \bullet \vec{r} e^{i\vec{k}\bullet\vec{r}} \right| n \right\rangle \left\langle n \left| \vec{\epsilon}' \bullet \vec{r} e^{i\vec{k}'\bullet\vec{r}} \right| 0 \right\rangle}{\hbar\omega_k - \left(E_n - E_0\right) - i\Gamma}$$

We see that the scattering is sensitive to the electronic structure of the ground- and intermediate states and to the polarization of the incoming and outgoing photons (see Fig. V.6 a). The existence of a "core-hole" in the intermediate state is responsible for introducing the linewidth parameter Γ, representing the lifetime of the state $|n>$.

a)

b)

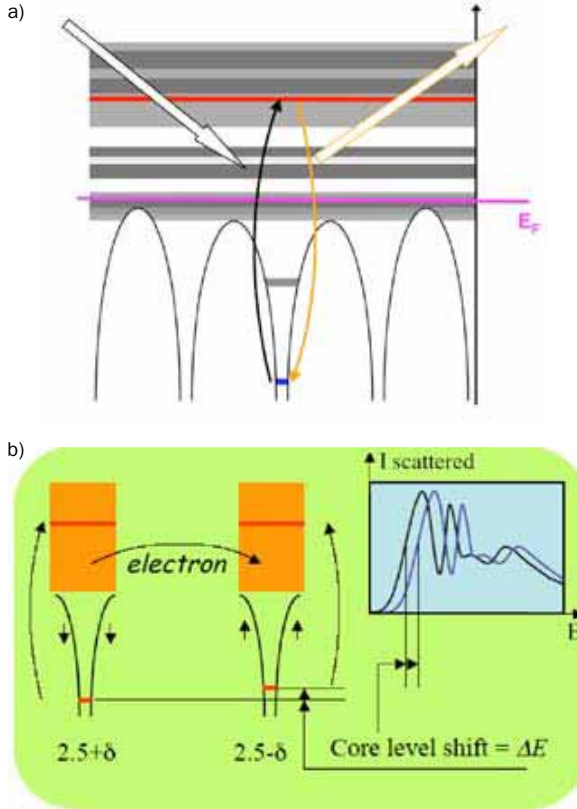2.5+δ   2.5-δ   Core level shift = ΔE

Fig. V.6. a) The resonant elastic scattering process, indicating a virtual transition from an occupied core state (blue) to an unoccupied intermediate valence state (red) [8]. b) A charge-dependent shift in the core-level energy shifts the energy-dependent scattering profile, providing contrast for charge-ordering [9].

For soft X-rays, where the photon wave-vector k is significantly larger than the atomic dimensions, one can expand the exponentials into dipole, quadrupole and octupole terms:

$$\langle 0|\vec{\epsilon}\bullet\vec{r}e^{i\vec{k}\bullet\vec{r}}|n\rangle \approx \langle 0|\vec{\epsilon}\bullet\vec{r}|n\rangle + i\langle 0|(\vec{\epsilon}\bullet\vec{r})(\vec{k}\bullet\vec{r})|n\rangle - \langle 0|(\vec{\epsilon}\bullet\vec{r})(\vec{k}\bullet\vec{r})^2|n\rangle.$$

The product of two such matrix elements yields a hierarchy of tensorial terms: dipole-dipole (rank 2), dipole-quadrupole (rank 3), quadrupole-quadrupole (rank 4), etc. These tensorial components can be enhanced by a suitable choice of polarizations and scattering vector.

In TMOs, interesting resonances are the L_2 and L_3 transition-metal edges, which connect filled $2p$ and unfilled $3d$ states. The corresponding photon wavelength, approximately one nm, allows the observation of resonant soft-X-ray *diffraction*, and the dependence of the matrix elements on valence-band electronic structure produces superstructure Bragg reflections, corresponding, for example, to *orbital-ordering* in the correlated-electron material. And when circularly-polarized X-rays are used, XMCD-contrast (see Chapter I) makes *mag-*

netic order visible. Finally, a charge-dependent shift of the initial core level shifts the energy-dependent resonant scattering profile (see Fig. V.6 b), providing a *charge-order* contrast.

One should note that soft-X-ray resonant diffraction is not easy: it requires scanning of the incoming photon energy, a multi-axis diffractometer in vacuum, and perhaps polarization-analysis of the scattered beam.

With the SwissFEL, a pump-probe resonant diffraction experiment can follow, for example, the melting of orbital order by a laser pump pulse and its recovery at later times. Its short pulses and flexible energy tuning, particularly near 1 nm wavelength, make the SwissFEL an ideal source for such investigations of TMO correlated electron materials. A particularly interesting application of pump-probe resonant elastic scattering at the SwissFEL would be the time-resolved study, at the nanometer scale, of so-called "orbitons", wave-like excitations of the orbitally-ordered phase, in manganites (see Fig. V.7).
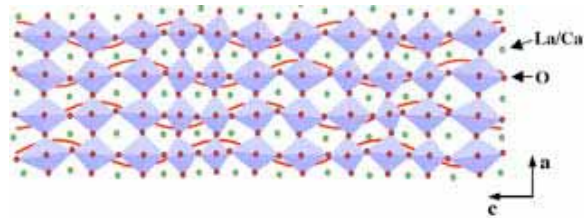

Fig. V.7. The proposed structure of an "orbiton", a wave-like excitation of the orbitally-ordered state in manganites. Optical pump-probe experiments provide evidence of its existence, with an oscillation period in the range of 10–50 ps [10]; resonant diffraction at the SwissFEL would allow its detailed study at the nanoscale.

Resonant inelastic X-ray scattering (RIXS)

We now lift the restriction to elastic scattering, by allowing $\omega = \omega_{k'} - \omega_k$ to be non-zero, requiring, in general, energy analysis of the scattered photons. A schematic of the RIXS process is shown in Figure V.8.
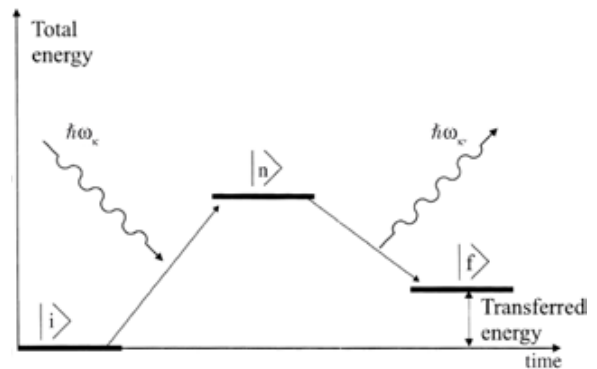

Fig. V.8. A schematic of the resonant inelastic X-ray scattering (RIXS) process.

A single-shot RIXS spectrometer

When performing resonant inelastic X-ray scattering (RIXS), the scattered intensity as a function of outgoing photon energy $E_{out} = \hbar\omega_{k'}$ is normally acquired for particular settings of the incoming energy $E_{in} = \hbar\omega_k$ by the monochromator. This is a procedure which is incompatible with single-shot operation at the Swiss-FEL. One would like to instantaneously obtain a two-dimensional plot of the scattered intensity as a function of E_{in}, E_{out}.

A method of performing single-shot RIXS has been proposed by V. Strocov [25] (see Fig. V.i2). The Swiss-FEL pulse is dispersed vertically by a monochromator (upper right in the figure) and brought to a line focus on the (homogeneous) sample. Scattered light corresponding to the various incoming photon energies is then focused to a vertical line and dispersed in E_{out} horizontally onto a CCD detector. The result is the desired two-dimensional plot.
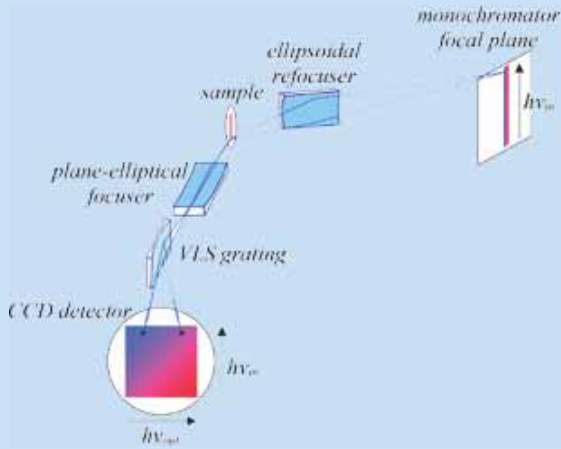

Fig. V.i2. Proposal for a doubly-dispersive RIXS spectrometer, suitable for use at the SwissFEL [25]. Advantages of this design include higher efficiency and compatibility with single-shot operation. The "VLS grating" has variable line spacing.

The scattering rate is now given by:

$$w = \frac{2\pi}{\hbar} \sum_f \left| \sum_n \frac{\langle f|H_2|n\rangle\langle n|H_2|i\rangle}{E_0 - E_n + \hbar\omega_k + i\Gamma} \right|^2 \delta\big((\hbar\omega_k - \hbar\omega_{k'}) - (E_f - E_i)\big).$$

Note the following features: a) The sensitivity to photon polarization and valence electronic states seen in resonant elastic scattering is also present for RIXS. b) Although there exists a (virtual) core-hole in the intermediate state, evidenced by the Γ-term in the denominator, because there is no hole in the final state, the $\omega_{k'}$ resolution of RIXS can in principle be infinitely good – as evidenced by the energy δ-function. c) Low-energy collective excitations, such as phonons, plasmons, spin-waves, etc., of the sample are accessible with RIXS, since what is measured is the energy *difference* between the incoming and outgoing photons. And since *two* photons are involved, the dipole selection rule $\Delta\ell=\pm1$ does not apply, such that a $d{\to}d$ transition can be observed (see Fig. V.9 a). d) Although performed at resonance, RIXS is a low-efficiency process: In resonant elastic

a)

b)
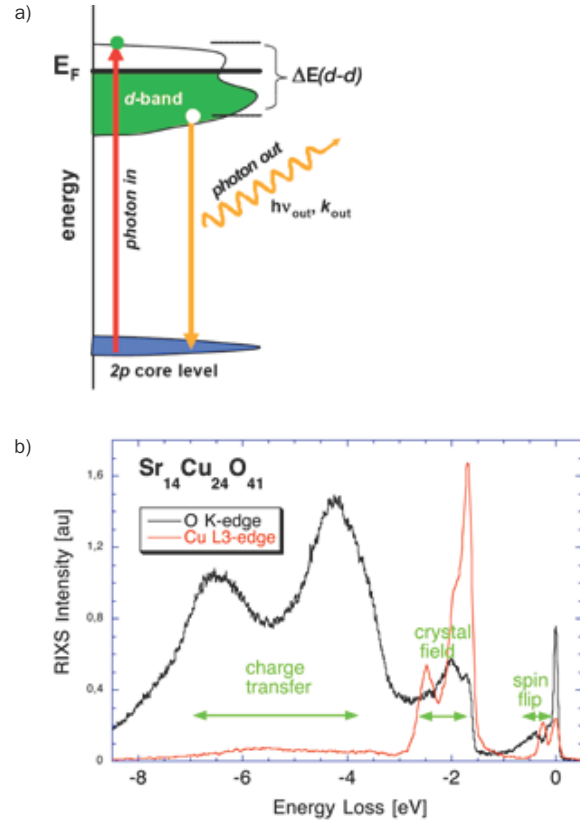

Fig. V.9. a) A $d{\to}d$ transition observable with RIXS, without restrictions from dipole selection rules. In this way, for example, the crystal-field or Jahn-Teller splitting of the d-orbitals of a 3d-transition-metal ion can be measured. b) Experimental RIXS spectra for $Sr_{14}Cu_{24}O_{41}$, taken at the oxygen K-edge and at the Cu L_3-edge [11], showing structures due to the transfer of charge between atoms, the Cu crystal-field splitting and collective spin-flip excitations.

scattering, the excitation of each of the N scattering atoms can be coherently added, since there is a unique final state. This results in a scattering intensity proportional to N^2. For RIXS, because the virtual excitation of different atoms leads to different final states, the contributions add incoherently, resulting in an intensity proportional to N [7].

Performing RIXS is an extremely challenging undertaking, due to the low scattered intensity and because of the necessity of performing an energy (and scattering-angle) analysis of the scattered radiation. For pump-probe RIXS experiments at the SwissFEL, it would therefore be particularly interesting to realize a single-shot mode of measuring, either in the frequency (see Infobox) or in the time (ditto) domains.

The intermediate scattering function

At the beginning of this Section, we saw how the transition rate for X-ray photon scattering, with momentum transfer $\vec{Q}$ and energy transfer $\hbar\omega$, is related to the scattering function $S(\vec{Q},\omega)$. This function shows peaks as a function of ω corresponding, for example, to long-lived oscillations (quasiparticles), such as phonons, spin-waves, etc. But finite lifetime effects will broaden these quasiparticle peaks, and in the limit of strong damping, it may be advantageous to observe the time-dependent fluctuations of the system directly – i.e., to measure instead the so-called time-domain or intermediate scattering function [12]:

$$S(\vec{Q},t) = \int_{-\infty}^{\infty} S(\vec{Q},\omega)e^{i\omega t}d\omega.$$

The intermediate scattering function basically provides the correlation time (over which $S(Q,t)$ decays to the value $1/e$) for the equilibrium fluctuations of a system, as a function of the fluctuation length scale $1/Q$. By monitoring the scattered intensity $I(\theta,t)$ at a particular scattering angle 2θ (related to the momentum-transfer by $Q = 4\pi \sin\theta/\lambda$), one has access to $S(Q,t)$ via the intensity correlation function $g_2(\theta,t)$ and the "Siegert relation" [13]:

$$g_2(\theta,t) \equiv \frac{\langle I(\theta,t)I(\theta,t+\tau)\rangle}{\langle I(\theta,t)\rangle^2} = 1 + \left|S(\vec{Q},t)\right|^2.$$

A measurement of $I(\theta,t)$ on the ultrafast time scale, pertinent to correlated electron materials, would require reading out a detector at an impossible rate of GHz -THz. Two realistic alternatives, however, which are well-suited to the characteristics of the SwissFEL, are provided by the "split-pulse" and "Mössbauer filter foil" techniques and are described in Infoboxes.

RIXS in the time-domain

A principal drawback of conventional RIXS measurements is the necessity of a fine energy-analysis of the scattered radiation, resulting in a significant loss of intensity. It has been suggested [26] that the ultrashort pulses of the SwissFEL could be used to effectively perform RIXS in the time-, instead of the energy domain.

If a suitable non-linear (NL) optical medium for soft X-rays could be developed, one could imagine performing X-ray heterodyne spectroscopy: A SwissFEL pulse is split into two pulses. One of these is scattered by the sample, causing the creation, by inelastic scattering, of multiple frequency components. This multi-frequency pulse is then recombined with the unscattered reference pulse in the NL-medium, where sum and difference frequencies are generated. The difference frequencies appear at the detector as slow oscillations, corresponding to the inelastic energy loss or gain in the sample.

Heterodyne spectroscopy is routinely performed with optical pulses, using the frequency-resolved optical gating (FROG) technique (see Fig. V.i3). Realization of an X-ray FROG will require the transform-limited pulses which a seeded SwissFEL will provide.
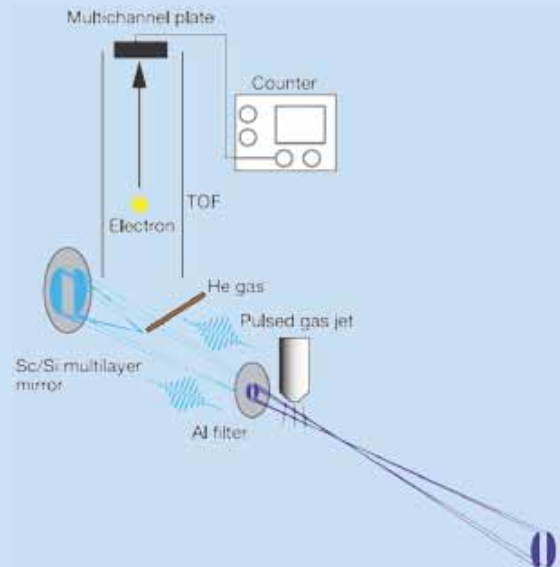
Fig. V.i3. A FROG device, using two-photon ionization in He gas as a NL mixer, which operates at a photon energy of 28 eV [27].

Split-pulse XPCS

X-ray photon correlation spectroscopy measures the time-correlation function of the coherently-scattered radiation intensity from a fluctuating sample:

$$g_2(\tau) = \frac{\langle I(t) I(t+\tau) \rangle}{\langle I(t) \rangle^2}.$$

Since this requires a detector bandwidth which exceeds that of the fluctuations, one is generally limited to times τ longer than 10 nsec.

The use the SwissFEL to probe ps-dynamics will require a different approach – "split-pulse XPCS" (see Fig. V.i4) [11]. Here a single SwissFEL pulse is split and delayed, producing a pair of pulses with tunable separation τ. The 2d-detector then registers a double-exposure speckle pattern, and the speckle contrast will decrease when τ exceeds the fluctuation correlation time τ_c.
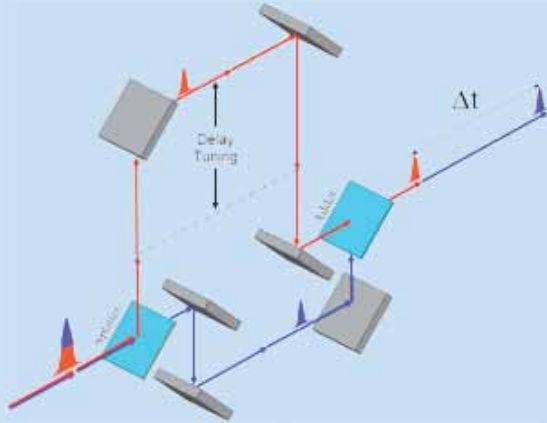

Fig. V.i4. A conceptual "split-and-delay" unit for XPCS at the SwissFEL [28].

That one indeed can measure $g_2(\tau)$ with split-pulse XPCS has been demonstrated by Gutt et al. [29]: The double exposure delivers the intensity $S(\tau) = I(t) + I(t+\tau)$, and the speckle contrast is given by the variance:

$$c_2(\tau) \equiv \frac{\langle S^2(\tau) \rangle - \langle S(\tau) \rangle^2}{\langle S(\tau) \rangle^2}$$

We note that:

$$\langle S^2(\tau) \rangle = 2\langle I^2 \rangle + 2\langle I(t) I(t+\tau) \rangle$$

$$\langle S(\tau) \rangle^2 = 4\langle I \rangle^2$$

and that, for a fully coherent beam,

$$\langle I^2 \rangle - \langle I \rangle^2 = \langle I \rangle^2.$$

We thus obtain:

$$c_2(\tau) = \frac{\langle I(t) I(t+\tau) \rangle}{2\langle I \rangle^2} = \frac{g_2(\tau)}{2}.$$

The Mössbauer filter-foil technique

The Mössbauer filter-foil technique provides an alternate method for measuring the intermediate scattering function [30]. Foils containing a stable Mössbauer isotope are placed in front of and behind the scattering sample and, at time $t=0$, a resonant Swiss-FEL pulse excites the isotope. The subsequent decay is then monitored by the total transmitted counting rate, measured in the forward direction (see Fig. V.i5).
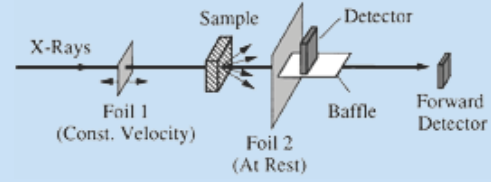

Fig. V.i5. The Mössbauer filter-foil method for measuring the intermediate scattering function $S(Q,t)$ [30].

Denoting by $\rho(Q,t)$ the spatial Fourier transform of the electron density in the sample at the time t, the intermediate scattering function is given by $S(Q,t) = \langle \rho(Q,0) \rho*(Q,t) \rangle$. Further, we let $|g(t)|^2$ denote the decay probability of the Mössbauer isotope a time t after excitation.

The signal $I(t)$ at the detector is the square of the coherent sum of the probability amplitudes for a) radiation scattered by the sample at time zero and emitted by the nuclei of the second foil at time t and b) emitted by the first foil at time t and directly scattered into the detector:

$$I(t) = \langle |\rho(Q,0) g(t) + g(t)\, \rho(Q,t)|^2 \rangle$$

$$= 2|g(t)|^2 \left[|\rho(Q,0)|^2 + R_e\, S(Q,t) \right]$$

From this expression, the intermediate scattering function can be extracted.

By far the most popular Mössbauer isotope is ^{57}Fe, with a resonant energy of 14.4 keV and an excited state lifetime of 141 ns. An upgrade option for the SwissFEL will make this photon energy accessible with the fundamental undulator radiation, as well as still higher energies using XFEL harmonics [31].

Advantages of the filter-foil method in combination with the SwissFEL are: a) extremely intense X-ray pulses with zero background during the nuclear decay, and b) measurements of $S(Q,t)$ for times far longer than those accessible with the split-pulse XPCS method. (The maximum feasible split-pulse delay will be ns for hard X-rays and tens of ps for soft X-rays.)

Origin of the metal-insulator transition in TaS₂

A signature feature of correlated electron materials is the occurrence of metallic and insulating phases, and of transitions between them. These metal-insulator transitions (MIT), can be caused by temperature, pressure, doping, or by other external influences. Two possible mechanisms for such an MIT are a) the Peierls instability and b) the Mott-Hubbard transition.

The Peierls instability

The Peierls instability [14] causes a metal to become an insulator by the action of a lattice distortion which doubles the crystal unit cell (see Fig. V.10). The energy cost incurred by the elastic distortion is more than compensated by a lowering of the electronic energy, due to the opening of a Peierls gap at the electronic Fermi level. Note that the situation is similar to that for the *spin* Peierls effect, discussed in Chapter I, where it is the lowered *magnetic* energy for spin dimers which drives the lattice distortion. Both the charge Peierls instability and the spin Peierls effect are intimately connected to the motion of lattice atoms, hence the relevant time scale will be that of lattice vibrations (i.e., 10–100 fs).
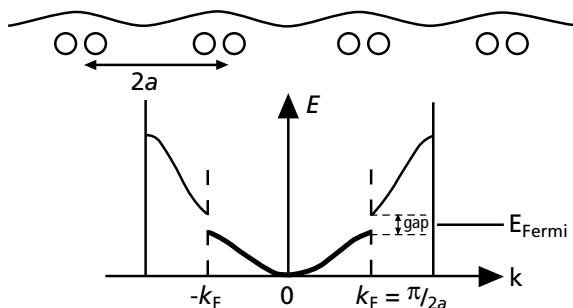

Fig. V.10. The Peierls instability [14]. Under special circumstances, it may become energetically favorable for a metallic crystal to undergo a spontaneous lattice distortion, forming atomic dimers, and doubling the crystal unit cell. In reciprocal space, the Brillouin zone is halved, and a gap opens at the Fermi level, causing a lowering of the electronic energy, which more than compensates for the cost in elastic energy. The presence of the gap causes the material to become insulating.

The Mott-Hubbard transition

A purely electronic mechanism for producing a metal-insulator transition results from the correlation physics described by the Hubbard model (see Infobox). In this model, the motion of electrons among lattice sites is governed by the two parameters U and W. The on-site

Coulomb repulsion U is the energy cost incurred when a lattice site is simultaneously occupied by two electrons. The bandwidth W measures the tendency of electrons to minimize their kinetic energy by delocalizing among the lattice sites. As shown in the Infobox, a large U/W ratio favors electron localization and hence the insulating state, while a small value for this ratio causes the electrons to become itinerant and the material to become a conductor. Therefore, at some intermediate value of U/W, an originally half-filled conduction band will split into two bands, by the creation of a Hubbard correlation gap (of order U) in the electron density of states (see Fig. V.11). Since no atomic motion is involved, the relevant time scale of the Mott-Hubbard transition is that of the electronic motion, i.e., 10 fs and faster.
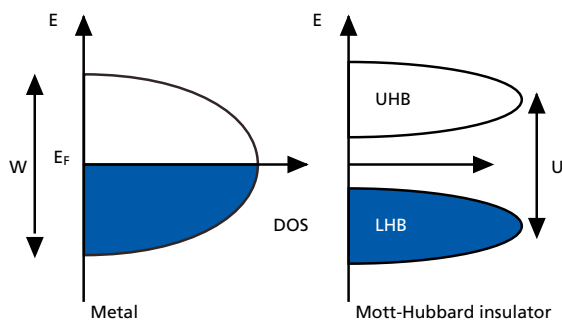

Fig. V.11. The Mott-Hubbard metal-insulator transition, as predicted by the Hubbard model, is a purely electronic effect, which opens a gap at the Fermi level, splitting the half-filled valence band into a filled "lower Hubbard band" (LHB) and an unfilled "upper Hubbard band" (UHB).

The characteristic time scales of the "slow" Peierls instability and the "fast" Mott-Hubbard transition are compared with electronic and lattice motions in Figure V.12.
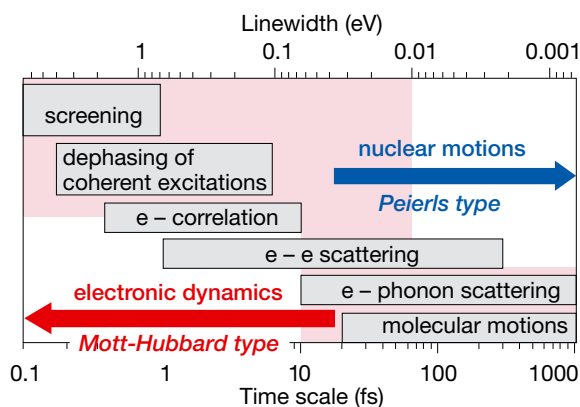

Fig. V.12. Characteristic time scales involved in metal-insulator transitions of the Peierls and Mott-Hubbard types. A Mott-Hubbard transition, being purely electronic in nature, is inherently faster than a Peierls transition, which is tied to the slower motion of the lattice atoms [15].

The Hubbard Model

The Hubbard Model [32] is the simplest model of interacting particles in a lattice and the starting point of many descriptions of correlated electron systems. It is based on the "Hubbard Hamiltonian":

$$H = -W \sum_{\langle ij \rangle \sigma} c_{j\sigma}^{\dagger} c_{i\sigma} + U \sum_{i} n_{i\uparrow} n_{i\downarrow}$$

Where the operators $c_{j\sigma}^{\dagger}$ and $c_{i\sigma}$ are electron creation and annihilation operators, $n = c^{\dagger}c$ is the number operator, and the sums run over the spin directions $\sigma = \uparrow$ and $\downarrow$ and the N lattice sites of the model. $\langle ij \rangle$ implies neighboring lattice sites. The principal parameters of the model are U and W, the on-site Coulomb repulsion and the electron bandwidth (or hopping rate), respectively. Let us consider two limiting cases [33]:

a) Static electrons ($W = 0$)
It is now enough to take into account a single site, and the possible states are $\{|0\rangle, |\uparrow\rangle, |\downarrow\rangle, |\uparrow\downarrow\rangle\}$, i.e., empty, a single spin up, a single spin down, or doubly-occupied. We calculate the partition function Z and the thermally-averaged site occupancy $\langle n \rangle$:

$$Z = \sum_{\alpha} \langle \alpha | e^{-\beta(H-\mu n)} | \alpha \rangle = 1 + e^{\beta\mu} + e^{\beta\mu} + e^{-\beta U + 2\beta\mu}$$

$$\langle n \rangle = \frac{1}{Z} \sum_{\alpha} \langle \alpha | (n_{\uparrow} + n_{\downarrow}) e^{-\beta(H-\mu n)} | \alpha \rangle = \frac{1}{Z} \left[0 + e^{\beta\mu} + e^{\beta\mu} + 2e^{-\beta U + 2\beta\mu} \right]$$

$$= \frac{2 \left(e^{\beta\mu} + e^{-\beta U + 2\beta\mu} \right)}{1 + 2e^{\beta\mu} + e^{-\beta U + 2\beta\mu}}$$

where $\beta = 1/k_B T$, and $\mu \equiv \dfrac{\partial E}{\partial n}$ is the chemical potential. Plotting $\langle n \rangle$ as a function of μ (Fig. V.i6) we find that at the condition for half-filling, $\langle n \rangle = 1$, the energy required to add an electron to the system changes by U. It is this "Hubbard gap" which implies an *insulating* behavior.
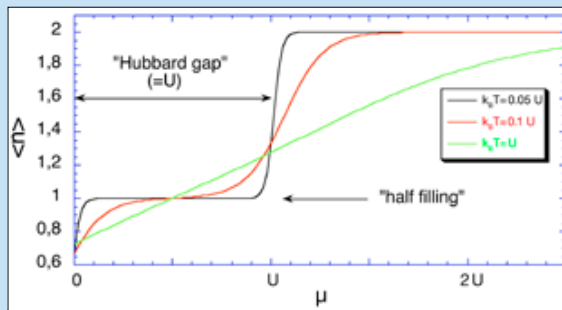
Fig. V.i6. Average site occupancy $\langle n \rangle$ vs. the chemical potential μ, for the Hubbard model without electron hopping ($W = 0$). The jump in μ by the value U at half-filling implies the existence of an energy gap, and hence insulating behavior.

b) Non-interacting electrons ($U = 0$)
In this case, it is convenient to use the reciprocal-space representation of the electron operators:

$$c_{k\sigma}^{\dagger} = \frac{1}{\sqrt{N}} \sum_{l} e^{ik \cdot l} c_{l\sigma}^{\dagger},$$

where k takes the values $k_n = 2\pi n/N$, assuming periodic boundary conditions in one dimension. The Hubbard Hamiltonian now has the form:

$$H = \frac{-W}{N} \sum_{k,k'} \sum_{l,l'\sigma} e^{ik \cdot l} e^{-ik' \cdot l'} c_{k\sigma}^{\dagger} c_{k'\sigma} = -2W \sum_{k\sigma} n_{k\sigma} \cos k,$$

where the last expression follows from performing the lattice sums. The energy levels of this Hamiltonian show a "band" behavior (see Fig. V.i7). As N goes to infinity, we obtain a (gapless) continuum of states, with bandwidth $4W$, which, at half-filling, implies *metallic* behavior.
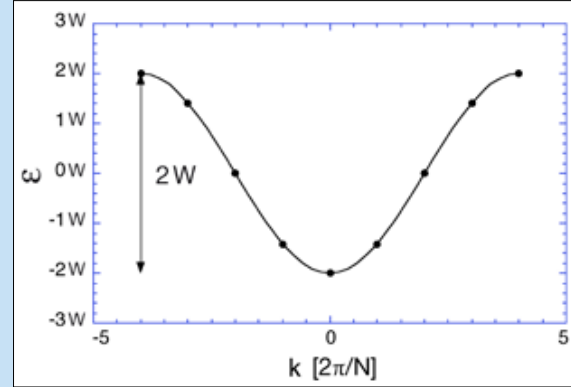
Fig. V.i7. Energy eigenvalues for the Hubbard Hamiltonian for non-interacting electrons ($U = 0$). The points are for a model with $N = 8$ lattice sites. Half-filling of such a continuous band implies conducting behaviour.

We thus find that the Hubbard Hamiltonian describes an insulator, in the case $W = 0$, and a metal, for $U = 0$. Between these two limits, i.e., for intermediate U/W, there must occur a *metal-insulator* transition: the *Mott transition*.

A particularly interesting material in which to investigate the nature of MIT is the 1T phase of the dichalcogenide tantalum disulfide [16]. $1T\text{-}TaS_2$ consists of S-Ta-S layers which are weakly coupled to one another and which, at room temperature, show an incommensurate charge-density wave (CDW) modulation which serves to split the Ta d-electron states into three bands. Since the uppermost of these is half-filled, the material is metallic. Below 180 K, the CDW locks to the lattice, and the resistivity increases by a factor 10. In order to investigate the nature of the MIT in this material, Perfetti et al. performed a pump-probe experiment on an insulating sample at T = 30 K. A 1.5 eV laser pump pulse, with a duration of 80 fs, excites hot electrons in the material, and at a variable time later, the time-resolved band structure is probed with angle-resolved photoemision, using 6 eV incoming photons.

Without a pump signal, or with a long (4.5 ps) pump-probe delay, the photoelectron spectra (see Fig. V.13 a), show a pronounced "lower Hubbard band" (LHB), corresponding to the insulating phase. But shortly after the pump, the LHB intensity collapses, and a tail appears, extending far above the Fermi level, demonstrating short-lived metallic behavior. The time-dependent LHB peak height (Fig. V.13 b) shows the ultrafast (fs) nature of the collapse and a continuous recovery of the insulating state. Both these observations argue strongly for a predominantly Mott-Hubbard nature of the MIT in $1T\text{-}TaS_2$.

Pump-probe photoelectron spectroscopy is not a technique which is particularly well-suited to the SwissFEL, due to the degraded energy resolution from the space-charge felt among the many low-energy photoelectrons which are simultaneously emitted from the sample. But other powerful X-ray methods, in particular photon-in-photon-out techniques, such as X-ray absorption near-edge spectroscopy (XANES) (see Chapter II) and resonant inelastic X-ray scattering (RIXS), can provide similar information pertinent to electronic band structure effects. These can be performed in a pump-probe arrangement, perhaps even in a single-shot mode (see Infobox), at the SwissFEL.
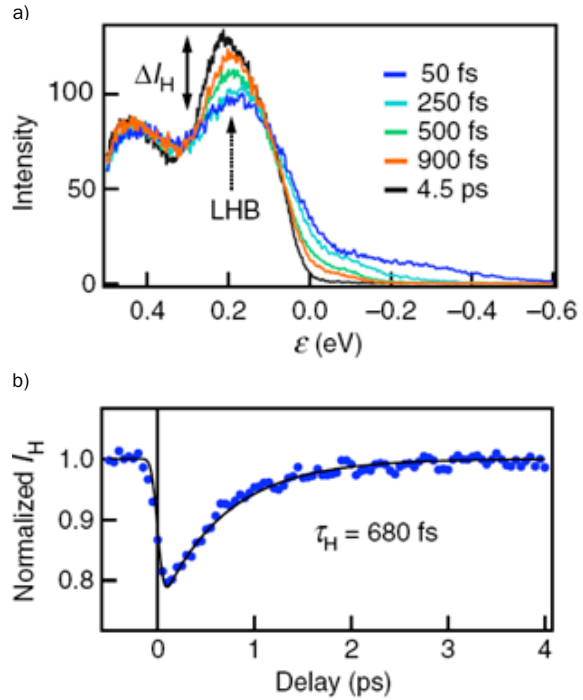

Fig. V.13. Time-resolved pump-probe photoelectron spectroscopy spectra for insulating $1T\text{-}TaS_2$, showing the ultrafast collapse of the lower Hubbard band and its continuous recovery, with a 680 fs time constant. These observations confirm the Mott-Hubbard nature of the metal-insulator transition in this material [16].

Ultrafast investigations of the electron-phonon interaction

Two of the most important aspects of the correlated electron chimera (Fig. V.1 b) are the electron and lattice degrees of freedom. One example of the electron-lattice interaction is the Peierls instability, discussed in the previous Section. Another is the phonon-mediated mechanism responsible for the creation of Cooper pairs in the BCS theory of (conventional) superconductivity. As evidenced by the following two examples, insight into this important interaction can be won through the use of ultrafast time-resolved measurement techniques.

Electron pump – lattice probe

Let us feed the electron part of the chimera and see how the lattice part reacts. A convenient system for such studies is elemental bismuth, with its interesting crystal structure and lattice dynamics, together with a high atomic number, suitable for hard X-ray scattering. The Bi lattice structure is shown in Figure V.14, where the pair of atoms in each unit cell is indicated, with a separation along the c_3 axis described by the coordinates x = $(0.5 \pm 0.0332)\, a_0$, where a_0 is the rhombohedral lattice constant. The deviation of these values from $a_0/2$ is due to the Peierls instability discussed earlier. The atoms of a pair vibrate against one another in the A_{1g} optical phonon mode, with a frequency of 2.9 THz.
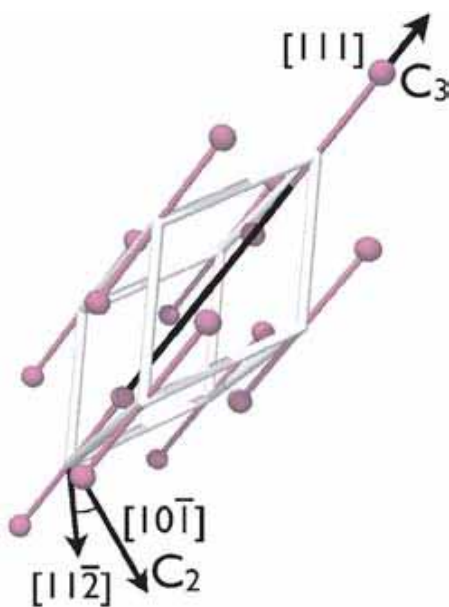

Fig. V.14. The rhombohedral crystal structure of bismuth, showing the positions of the two atoms per unit cell along the three-fold c_3 axis.

An ultrafast laser pulse excites the electronic system in Bi, altering its electronic state and, via the electron-phonon interaction, causes a sudden (i.e., on the electronic time-scale) weakening of the interatomic potential – due to the partial occupation of normally unoccupied anti-bonding orbitals (see Fig. V.15 a). As a result, the (slowly-moving) atoms no longer find themselves at potential minima, and they begin to oscillate coherently in the A_{1g} phonon mode. This displacive excitation oscillation has been *directly* observed with pump-probe hard-X-ray diffraction at the laser-sliced FEMTO beamline at the SLS synchrotron (see Fig. V.15 b) [17]. The dependence of the interatomic potential on the degree of electronic excitation was determined in this experiment by observing a linear drop in the phonon frequency with increasing pulse fluence (inset in Fig. V.15 b), in excellent quantitative agreement with density functional theory calculations (see Fig. V.16 a) [18, 19].
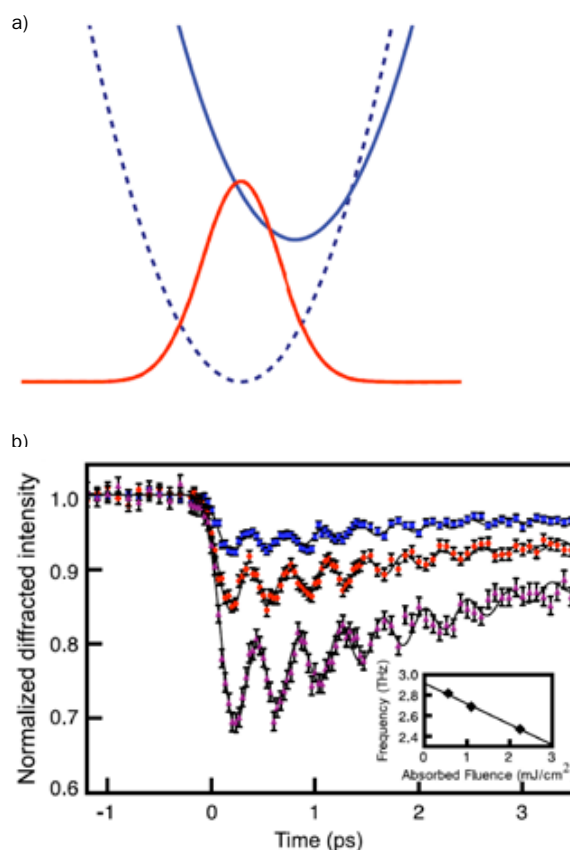
a)

b)

Fig. V.15. a) Displacive excitation of coherent phonons. Upon optical excitation, the interatomic potential becomes shifted and softer (blue dashed → blue solid), causing the equilibrium atomic distribution (red) to adapt accordingly. b) The displacive excitation of A_{1g} optical phonons in Bi is performed with a laser pump pulse and probed with hard X-ray diffraction at the FEMTO beamline of the SLS synchrotron [17]. With increasing levels of excitation, a mode softening is observed due to the electron-phonon interaction.
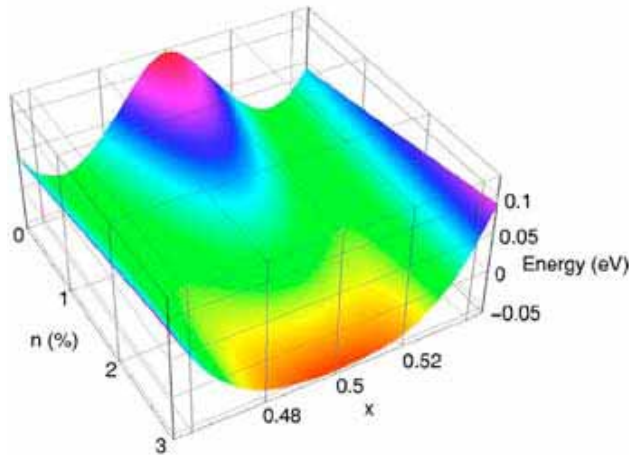
Fig. V.16. The density functional theory prediction of the interatomic potential for the A_{1g} optical phonon mode in Bi, as a function of the atomic coordinates x and the percentage of excited valence electrons n [18]. Note the softening (and symmetrization) which occurs upon increasing excitation.

With the extremely low flux at the laser-sliced FEMTO beamline (see Chapter II), each point in Figure V.15 b requires typically one minute of measurement time; with a more weakly scattering system than bismuth, this time increases by orders of magnitude. The ultra-high peak brightness of the SwissFEL, together with its 100–400 Hz repetition rate and the virtually continuous tuning of the pump-probe delay, will allow detailed investigations of subtle diffraction features from technologically interesting but weakly scattering materials.

Lattice pump – electron probe

We have seen how pumping the electron part of the correlated electron chimera influences the lattice. Can we also perform the inverse? In a purely optical experiment, Rini et al. have excited a particular phonon mode in a perovskite manganite and recorded the effect on the electron system [20].

With the replacement of Pr by the smaller Ca ion, the crystal structure of $PrMnO_3$ undergoes a local tilt of the MnO_6 octahedra, in the form of an orthorhombic distortion (see Fig. V.17). The electron hopping from Mn to Mn proceeds via an oxygen-mediated super-transfer mechanism, which depends on the orbital overlap between neighboring sites, and this overlap is sensitive to the octahedron tilt. Hence the distortion causes a decrease in the Hubbard model bandwidth parameter W, therefore giving rise to an insulating phase. Indeed, orthorhombic $Pr_{1-x}Ca_xMnO_3$ is insulating over a wide range of compositions and temperatures.
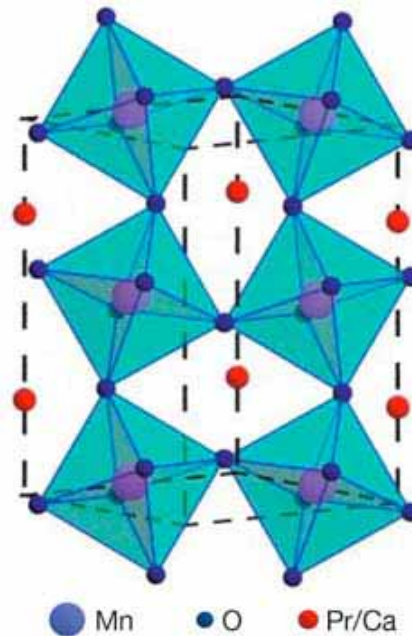

Fig. V.17. Ca-doping causes $Pr_{1-x}Ca_xMnO_3$ to orthorhombically distort, resulting in reduced orbital overlap ($\sim W$) and hence in insulating behavior [20].

At a phonon energy of 71 meV ($\nu = 17.2$ THz, in the mid-IR), the Mn-O distance in $Pr_{0.7}Ca_{0.3}MnO_3$ undergoes a periodic modulation, implying also a modulation in the Hubbard bandwidth W: one can hence envisage a dynamic metal-insulator transition. Rini et al. searched for this effect by performing an IR-pump / visible-probe experiment [20], using the reflectivity of visible light to query the electron system. Their results are shown in Figure V.18. Note that IR-excitation leaves the system in its electronic ground-state.
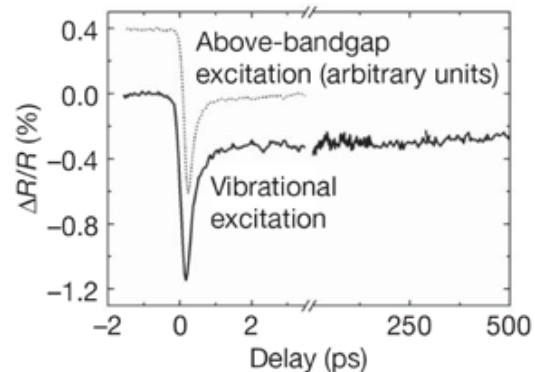

Fig. V.18. The ultrafast change in reflectivity (at 800 nm wavelength) observed after excitation of an IR phonon mode in $Pr_{0.7}Ca_{0.3}MnO_3$ [20]. The effect is very similar to that produced by a visible laser pump (dotted curve), demonstrating that it indeed represents a transient change to a metallic state.

Using the visible reflectivity as a probe of electronic structure implies that one is sensitive only to changes in the immediate vicinity of the Fermi energy. A more complete probe of local and cooperative electronic effects is possible using soft-X-ray spectroscopies such as XANES and RIXS. Hence an IR-pump / soft-X-ray probe experiment at the SwissFEL has great potential for delivering a detailed picture of this type of dynamic MIT.

A multitude of further possibilities exist for SwissFEL-based pump-probe investigations of the correlated-electron chimera. We have seen that resonant soft-X-ray diffraction and inelastic scattering are sensitive to charge-, magnetic-, and even orbital-order, and the suggestion has been made that with a suitable pump pulse, one can melt the order and monitor its recovery. One could also excite and detect cooperative excitations of these ordered phases, such as orbitons [10], with resonant frequencies in the THz regime, accessible to the SwissFEL. Another possibility [21] is to use photo-excitation to effectively change the filling number, i.e., "photo-doping" the correlated electron system, and to use the SwissFEL to detect the resulting effects on the lattice and electronic systems.

Complexity in correlated electron materials

In a much cited paper, Dagotto [22] discusses the concept of *complexity* in connection with correlated electron materials. The essential point is that the competition between the charge-spin-orbital-lattice degrees of freedom can lead to the coexistence of different phases which are virtually degenerate in energy, and hence to inhomogeneities and glassy dynamics on a wide range of length and time scales.

A hallmark of such "complex matter", which exists "at the edge of chaos", is a non-linear "giant" response to a small perturbation. For example, charge transport in manganite TMOs is different from that in simple metals: an isolated charge may strongly perturb its local environment, inducing the creation of a polaron, which may then attract other polarons to form larger, long-range structures. The manganite phase diagram was shown in Figure V.4 a, with the close juxtaposition of ferromagnetic metal (FM) and antiferromagnetic insulator (AFI) phases. The complexity view of the magnetic-field-induced metal-insulator transition in this material is that a ground state exists with quenched disorder, arising perhaps from lattice distortion accompanying chemical doping (see Fig. V.19 a), with a glassy intermixture of FM and AFI phases (see Fig. V.19 b). A small applied magnetic field is then sufficient to tip the energy balance in favor of the FM phase, causing a giant, percolative change in the bulk conductivity.
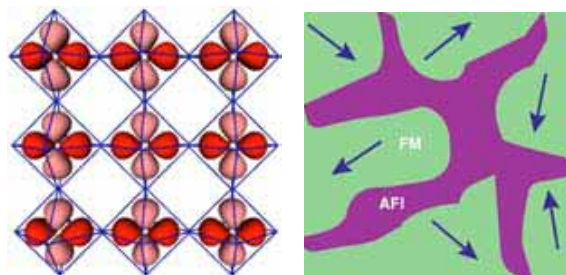

Fig. V.19 a) Lattice strain, e.g., arising from fluctuations in chemical doping, produces a slight local preference for a particular phase [23]. b) On a coarser scale, a small external perturbation, such as an applied magnetic field, can cause a non-linear, "giant" percolative change in the macroscopic conductivity [22].

Also the cuprate superconductors show a variety of nanoscale inhomogenieties (see Fig. V.20), including the charge-spin stripes mentioned at the beginning of this Chapter (see Fig. V.5 b). Although the importance of stripes to the mechanism of high-temperature superconductivity is in question, also these materials appear to exhibit a giant response: A S–N–S (superconductor –
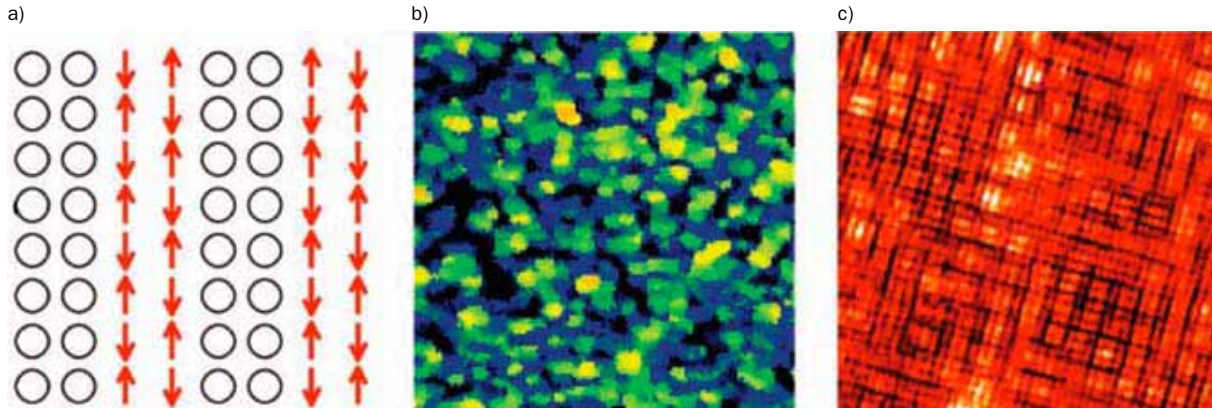
Fig. 20. Examples of nanoscale inhomogeneity in highly-correlated cuprate TMOs [22]. a) Idealized charge/spin stripes in cuprate super-conductors, b) variations in the d-wave superconducting gap, detected in $Bi_2Sr_2CaCu_2O_{8+\delta}$ using scanning tunneling microscopy, c) a checkerboard charge-ordered state in a Na-doped cuprate.

normal conductor – superconductor) junction made of cuprate materials, whose N-layer thickness exceeds 100 coherence lengths, behaves as if it were a S-S Josephson junction, implying that the presence of neighboring superconducting material tips the balance in the thick N-layer to superconducting behavior [22].

In his paper, Dagotto draws parallels between correlated-electron materials and other forms of complex matter, such as polymers, liquid crystals and even bio-material. Just as groups of atoms in these soft materials form local solid patterns (i.e., molecules), which, when considered globally, exhibit complex, fluid behavior, so can, for example, Jahn-Teller-ordered regions in manganites lead to a complex electron liquid-crystal behavior, intermediate between an electron solid and an electron liquid. The analogy with biochemical systems (see Chapter IV) is striking: a large number of nearly degenerate states, with the corresponding entropic barriers, move on a rugged energy landscape. But a peculiarity of the electron-based complexity is that it is inherently quantum-mechanical [22].

The importance of the SwissFEL for investigating the spatial and temporal characteristics of such complex electron matter is twofold. Despite decades of work by a generation of scientists, a theoretical understanding of these materials is lacking. Fundamental approaches, like the Hubbard model (see Infobox), may be close to explaining microscopic features, such as the superconducting pairing mechanism, but they reach their limits when considering long-range interactions such as Coulomb and electron-lattice effects. Time-resolved struc-

tural and spectroscopic information from the SwissFEL may provide the experimental foundation for a new level of description of these materials, connecting microscopic mechanisms with macroscopic phenomenology, in the form of large-scale, numerical simulations. The second major SwissFEL contribution could be the development of practical applications of these fascinating materials: particularly relevant are dynamic effects such as non-linear switching between states of high and low conductivity, the coupling of magnetic and electric effects in the so-called "multiferroics" (see Infobox), dielectric effects in relaxor ferroelectrics and the development of oxide electronics, including TMO field-effect transistors and novel spintronic devices.

Summary

- *The charge, spin, orbital and lattice degrees of freedom of correlated electron materials lead to the inhomogeneous and dynamic coexistence of material phases with novel orderings. Prominent examples, the dynamic polarons in manganites and the charge-spin stripes in cuprates, have characteristic time and length scales (ps and nm) which are well-suited to be studied with the SwissFEL.*

- *Hard X-ray diffraction and the resonant soft-X-ray techniques of elastic diffraction and inelastic scattering provide high sensitivity to charge, spin, orbital and lattice degrees of freedom, in wavelength ranges covered by the SwissFEL. Furthermore, the SwissFEL will provide excellent access to the sub-ps dynamics of these degrees of freedom, either using laser-pump/X-ray probe experiments or by sampling equilibrium fluctuations via the intermediate scattering function $S(Q,t)$.*

- *Photoemission spectroscopy, a preferred technique for static studies of correlated electron materials in the laboratory and at synchrotrons, is poorly suited to time-resolved measurements at the SwissFEL, due to resolution degradation by electron space-charge effects. However, the sensitivity to electronic structure provided by the photon-in/photon-out X-ray absorption and resonant scattering techniques make them highly promising alternatives, particularly in single-shot mode.*

- *The nature of metal-insulator transitions in correlated-electron materials can be elegantly determined by time-resolved pump-probe experiments. In this way, the metal-insulator transition in $1T\text{-}TaS_2$ is shown, by its ultrafast character (i.e., much faster than typical lattice vibratons), to be due to the electronic Mott-Hubbard transition, and not to the lattice-related Peierls instability.*

- *The electron-phonon interaction can be directly studied in time-resolved pump-probe experiments. Examples are the creation via hot electrons of coherent phonons in bismuth and the triggering of a dynamic metal-insulator transition by the IR-excitation of a particular phonon mode in $Pr_{0.7}Ca_{0.3}MnO_3$.*

- *In many respects, correlated-electron materials exhibit electronic complexity, characterized by glassy dynamics and giant responses to small external perturbations. This complexity is reminiscent of that of molecular systems, such as liquid crystals and even biological macromolecules. The ability of the SwissFEL to provide novel information over a large range of time and length scales makes it an ideal tool to establish an experimental foundation for a unification in the theory of correlated electrons at the micro- and macro-scales.*

References

[1] Johnson, S., (private communication)

[2] Bednorz, J. G. & Muller, K. A., "Possible High-Tc Superconductivity in the Ba-La-Cu-O System," *Zeitschrift Fur Physik B-Condensed Matter* **64**, 189-193 (1986).

[3] Castleton, C. W. M. & Altarelli, M., "Orbital ordering in the manganites: Resonant x-ray scattering predictions at the manganese L-II and L-III edges," *Physical Review B* **62**, 1033-1038 (2000).

[4] Lynn, J. W., Argyriou, D. N., Ren, Y., Chen, Y., Mukovskii, Y. M. & Shulyatev, D. A., "Order and dynamics of intrinsic nanoscale inhomogeneities in manganites," *Physical Review B* **76**, 01443-7 (2007).

[5] Kivelson, S. A., Bindloss, I. P., Fradkin, E., Oganesyan, V., Tranquada, J. M., Kapitulnik, A. & Howald, C., "How to detect fluctuating stripes in the high-temperature superconductors," *Reviews of Modern Physics* **75**, 1201-1241 (2003).

[6] Als-Nielsen, J. & McMorrow, D. *Elements of Modern X-Ray Physics* (ed. Wiley) (2001).

[7] Altarelli, M., "Resonant x-ray scattering: A theoretical introduction", *Lect. Notes Phys.* **697**, 201-242 (2004).

[8] Lorenzo, J. E. (private communication)

[9] Joly, Y. (private communication)

[10] Ren, Y. H., Hu, Y. F., Li, Q., Hong, C. S., Hur, N. H. & Lupke, G. "Ultrafast collective dynamics of short-range charge/orbital ordering fluctuations in colossal magnetoresistive oxides", *cond-mat/0310360v1* (2003).

[11] Schmitt, Th. (private communication)

[12] Grubel, G., Stephenson, G. B., Gutt, C., Sinn, H. & Tschentscher, T., "XPCS at the European X-ray free electron laser facility," *Nuclear Instruments & Methods in Physics Research Section B-Beam Interactions with Materials and Atoms* **262**, 357-367 (2007).

[13] Goodman, J. W. *Statistical Optics* (Wiley Classics Library, 2000).

[14] Peierls, R. E. *Quantum Theory of Solids* (Oxford University Press, 2004).

[15] Wolf, M. (private communication)

[16] Perfetti, L., Loukakos, P. A., Lisowski, M., Bovensiepen, U., Wolf, M., Berger, H., Biermann, S. & Georges, A., "Femtosecond dynamics of electronic states in the Mott insulator 1T-TaS2 by time resolved photoelectron spectroscopy," *New Journal of Physics* **10**, 053019 (2008).

[17] Johnson, S. L., Beaud, P., Milne, C. J., Krasniqi, F. S., Zijlstra, E. S., Garcia, M. E., Kaiser, M., Grolimund, D., Abela, R. & Ingold, G., "Nanoscale depth-resolved coherent femtosecond motion in laser-excited bismuth," *Physical Review Letters* **100**, 155501(2008).

[18] Murray, E. D., Fritz, D. M., Wahlstrand, J. K., Fahy, S. & Reis, D. A., "Effect of lattice anharmonicity on high-amplitude phonon dynamics in photoexcited bismuth," *Physical Review B* **72**, 060301 (2005).

[19] Fritz, D. M., et al., "Ultrafast bond softening in bismuth: Mapping a solid's interatomic potential with X-rays," *Science* **315**, 633-636 (2007).

[20] Rini, M., Tobey, R., Dean, N., Itatani, J., Tomioka, Y., Tokura, Y., Schoenlein, R. W. & Cavalleri, A., "Control of the electronic phase of a manganite by mode-selective vibrational excitation," *Nature* **449**, 72-74 (2007).

[21] Cavalleri, A., (private communication)

[22] Dagotto, E., "Complexity in strongly correlated electronic systems," *Science* **309**, 257-262 (2005).

[23] Milhaly, L. http://solidstate.physics.sunysb.edu/talk/2004_dubrovnik2/.

[24] Cheong, S-W. & Mostovoy, M., "Multiferroics: a magnetic twist for ferroelectricity", *Nature Materials,* **6**, 13-20 (2007).

[25] Strocov, V., (private communication)

[26] Abbamonte, P., (private communication)

[27] Sekikawa, T., Kosuge, A., Kanai, T. & Watanabe, S., "Nonlinear optics in the extreme ultraviolet," *Nature* **432**, 605-608 (2004).

[28] Gutt, C., (private communication)

[29] Gutt, C., Stadler, L. M., Duri, A., Autenrieth, T., Leupold, O., Chushkin, Y. & Grubel, G., "Measuring temporal speckle correlations at ultrafast x-ray sources," *Optics Express* **17**, 55-61 (2009).

[30] Baron, A. Q. R., Franz, H., Meyer, A., Ruffer, R., Chumakov, A. I., Burkel, E. & Petry, W., "Quasielastic scattering of synchrotron radiation by time domain interferometry," *Physical Review Letters* **79**, 2823-2826 (1997).

[31] Palffy, A., "A Systematic Study of Nuclear Photoexcitation with X-Ray Laser Fields," *J. Modern Optics* **55**, 2603-2615 (2008).

[32] Hubbard, J., "Electron Correlations in Narrow Energy Bands," Proceedings of the Royal Society of London Series a-Mathematical and *Physical Sciences* **276**, 238 (1963).

[33] Scalettar, R. T., "Elementary Introduction to the Hubbard Model," http://leopard.physics.vcdavis.edu/rts/p210/hubbard7.pdf.